Multilayer Laue lenses at high X-ray energies: performance and applications

Murray, Kevin T.; Pedersen, Anders Filsøe; Mohacsi, Istvan; Detlefs, Carsten; Morgan, Andrew J.; Prasciolu, Mauro; Yildirim, Can; Simons, Hugh; Jakobsen, Anders Clemen; Chapman, Henry N.; Poulsen, Henning Friis; Bajt, Saša

Published in:
Optics Express

Link to article, DOI:
10.1364/OE.27.007120

Publication date:
2019

Document Version
Publisher's PDF, also known as Version of record

Research Article | Vol. 27, No. 5 | 4 Mar 2019 | OPTICS EXPRESS 7120
Optics EXPRESS

Multilayer Laue lenses at high X-ray energies: performance and applications

KEVIN T. MURRAY,[1] ANDERS F. PEDERSEN,[2] ISTVAN MOHACSI,[1] CARSTEN DETLEFS,[3] ANDREW J. MORGAN,[4] MAURO PRASCIOLU,[1] CAN YILDIRIM,[3,5] HUGH SIMONS,[2] ANDERS C. JAKOBSEN,[2] HENRY N. CHAPMAN,[4,6,7] HENNING F. POULSEN,[2] AND SAŠA BAJT[1,*]

[1]*DESY, Notkestrasse 85, 22607 Hamburg, Germany*
[2]*Department of Physics, Technical University of Denmark, 2800 Kgs Lyngby, Denmark*
[3]*European Synchrotron Radiation Facility, 71 Avenue des Martyrs, 3800 Grenoble, France*
[4]*Center for Free-Electron Laser Science, DESY, Notkestrasse 85, 22607 Hamburg, Germany*
[5]*OCAS, J. F. Kennedylaan 3, 9060 Zelzate, Belgium*
[6]*Department of Physics, University of Hamburg, Luruper Chaussee 149, 22607 Hamburg, Germany*
[7]*Centre for Ultrafast Imaging, Luruper Chaussee 149, 22607 Hamburg, Germany*
[*]*sasa.bajt@desy.de*

Abstract: X-ray microscopy at photon energies above 15 keV is very attractive for the investigation of atomic and nanoscale properties of technologically relevant structural and bio materials. This method is limited by the quality of X-ray optics. Multilayer Laue lenses (MLLs) have the potential to make a major impact in this field because, as compared to other X-ray optics, they become more efficient and effective with increasing photon energy. In this work, MLLs were utilized with hard X-rays at photon energies up to 34.5 keV. The design, fabrication, and performance of these lenses are presented, and their application in several imaging configurations is described. In particular, two "full field" modes of imaging were explored, which provide various contrast modalities that are useful for materials characterisation. These include point projection imaging (or Gabor holography) for phase contrast imaging and direct imaging with both bright-field and dark-field illumination. With high-efficiency MLLs, such modes offer rapid data collection as compared with scanning methods as well as a large field of views.

1. Introduction

Hard X rays with photon energies in the range of 15 keV to over 100 keV can be used to investigate the structures of materials for a wide range of applications [1, 2]. Thanks to the high penetration power of this radiation it is particularly attractive for the investigation of hierarchically organised materials including most metals, ceramics and rocks [3, 4], technologically relevant devices such as batteries and solar cells [5], and biological materials [6]. By mapping the structure of deeply-embedded crystalline elements in three dimensions at nanometer resolution one would be able to determine the influence of domain walls or defects on macroscale mechanical or physical structural properties, for example. This requires wavelengths short enough to Bragg-reflect from lattices of the material, combined with an imaging methodology to localise the origin of scattering. Such imaging can in principle be carried out by forming a tightly focused X-ray beam that is scanned relative to the sample to create maps of the strength of diffraction at particular scatting angles [7, 8], or to illuminate the sample and form a magnified image with a lens whose aperture is centered on a particular scattering angle [4]. For amorphous or soft-matter systems, phase contrast imaging with hard X rays allows high-resolution structural studies at reduced dose levels as compared with mapping or directly imaging the absorption of a sample.

While the images formed by scanning a probe or forming a magnified image can be equivalent,

#346496 https://doi.org/10.1364/OE.27.007120
Journal © 2019 Received 21 Sep 2018; revised 17 Feb 2019; accepted 17 Feb 2019; published 26 Feb 2019

Optics EXPRESS

due to reciprocity [8], the choice of the imaging modality may depend on considerations of the source, dose to the sample, speed of imaging, properties of the objective lens, and the specific question being addressed. Source brightness decreases sharply with photon energy, favouring the direct formation of a magnified image with hard X rays, due to the lower required coherence of the illumination. In either modality, the achievable spatial resolution is determined by the numerical aperture (NA) of the objective lens employed. Achieving a high NA for hard X rays is challenging due to the small interaction cross sections of this radiation with matter and consequently the small difference in refractive index between any material and vacuum. Optics that can achieve a spatial resolution or focussed spot diameter in the nanometer range include Kirkpatrick-Baez (KB) mirrors, compound refractive lenses (CRLs), and diffractive optical elements such as Fresnel zone plates (ZPs) [7, 9].

The imaging resolution of X-ray optical elements is usually determined by the precision to which they can be fabricated, but limitations also exist due to the optical properties of materials. For example, the NA of KB mirrors is limited by the critical angle of reflection unless the mirror is coated with a multilayer structure. A 2D focus of $12 \times 13\,\mathrm{nm}^2$ at 33.6 keV was recently reported [10]. KB mirrors are achromatic, but do not fulfill the Abbe sine condition and therefore are only suitable as a probe-forming objective rather than for full-field direct imaging [9]. The theoretical resolution limit of CRLs is also governed by optical properties, with a largest NA given by $\sqrt{2\delta}$ for a refractive index decrement δ [11]. At 20 keV this corresponds to NA $= 4 \times 10^{-3}$ or a resolution of 10 nm. Since for hard X rays and away from atomic resonances, δ is proportional to the square of the wavelength, the resolution (which depends on the wavelength divided by NA) remains approximately constant as the photon energy is increased. CRLs are chromatic (their focal length depends on wavelength), as are diffractive optics. To achieve nanometer focusing with diffractive elements requires diffracting structures whose size and placement accuracy are about the same size as the focus. At hard X-ray photon energies the diffracting structure must also be thick to ensure reasonable efficiency, which then requires structures that consist of nanometer spaced zones that are many micrometers thick. Such structures can be made by layer deposition, which are then sliced to create a multilayer Laue lens (MLL) [12]. MLLs have been fabricated that can create a beam focus of $8.4 \times 6.8\,\mathrm{nm}^2$ with 68 % diffraction efficiency at a photon energy of 16.3 keV [13].

Here we report on some of our investigations of the use and performance of MLLs in the hard X-ray regime (at photon energies up to 34.5 keV) where we explored various imaging modalities that may be useful in a variety of applications. At lower photon energies MLLs have been primarily utilised in scanning microscopy [14, 15], whereas here we concentrate on approaches that directly produce two-dimensional images. This parallel "full field" mode of detection offers faster data collection and does not need a scanning stage. We investigated projection imaging (also known as Gabor holography) for phase contrast imaging, and direct imaging with both bright-field and dark-field illumination. In this paper we first briefly describe the design and fabrication of the MLLs (Section 2). In Section 3, the experimental setup (Section 3.1) and the imaging geometries (Section 3.2) used for optics characterization and applications are presented. The results of the optical performance and diffraction efficiency of these lenses at two different photon energies (17.3 keV and 34.5 keV) are discussed in Section 4. This includes the analysis of the wavefronts of individual lenses, 2D focus analysis, and presentation of full field microscopy images obtained with these sets of lenses. The final section focuses on full field imaging and the future perspective is briefly outlined.

2. MLL fabrication and operation

MLLs can be prepared by depositing thousands of nanometer-thick layers onto a smooth substrate, alternating between a material of high atomic number and one of low atomic number [13]. An axisymmetric MLL, which images in two dimensions, can be prepared by depositing materials

Optics EXPRESS

onto a cylindrical wire [16]. However, MLLs are usually fabricated using plane substrates, since they can be obtained with the atomically-smooth surface needed to achieve a high-quality multilayer structure. In this case the MLL is a one-dimensional stack that operates like a cylindrical lens. Two orthogonally crossed lenses can then be used to image in two dimensions. The multilayers in this work were deposited using magnetron sputtering, but other methods can be used as well [17]. The layer thickness must follow the Fresnel zone plate equation to ensure that the path length from the face of the lens to the focal spot, located at a distance f from the intersection of the face of the lens with the optical axis, increases by $\lambda/2$ for each layer, where λ is the wavelength. For a thin ZP the height of the zone from the optical axis r_n of the n^{th} layer obeys $r_n^2 + f^2 = (f + n\lambda/2)^2$ [7]. For a thick zone plate, however, incident collimated rays diffracting from a point at a distance z from the front face of the structure must be deflected such that they achieve a focal length $f - z$. The distance r_n of the n^{th} layer from the optical axis can then be expressed as

$$r_n(z) \approx \underbrace{\sqrt{n\lambda f + \frac{n^2\lambda^2}{4}}}_{\text{ZP condition}} \underbrace{(1 - \frac{z}{2f + n\lambda/2})}_{\text{Bragg's law}} \tag{1}$$

where only the first two terms of a Taylor series of $r_n(z)$ are listed [18]. We see that the layers decrease in height r_n with increasing distance z in the direction of the optical axis, meaning that the layers are tilted. This is indeed the condition of Bragg diffraction. The angle of the tilt (for focusing of an incident collimated beam) is given by the Bragg angle θ, approximately equal to $r_n/(2f)$ for small angles. This curvature of $1/(2f)$ of the layers is equivalent to the imaging condition of a curved spherical mirror at normal incidence (creating a virtual image) or, more aptly, to that of a curved array of reflecting surfaces [19]. Figure 1(a) depicts the structure of a wedged MLL.

For a one-dimensional MLL fabricated with parallel (flat) layers, at least one of the layers can be placed in the Bragg-diffracting condition by tilting the entire MLL. The number of layers that will efficiently diffract depends on the angular acceptance of the layers—the Darwin width—which decreases linearly with the layer period [20]. The NA is in this case comparable to those of the optical systems mentioned in Sec. 1. Wedging the layers is necessary to achieve NA's in excess of 10^{-3}. This requires that the deposition rate of the materials varies with position on the substrate. The correct radius of curvature can be made by ensuring that the deposition rate linearly falls to zero over a width equal to $2f$, for example [21]. This can be prepared by placing a mask between the sputtering targets and the substrate during the deposition process [21–24]. It has been demonstrated that cutting out a slice of the multilayer at a position where the local gradient matches the $1/(2f)$ curvature gives an efficient MLL in which all layers are in the Bragg-reflecting condition [13, 21, 24]. To obtain high quality MLLs the multilayer deposition typically starts with the thinnest layers to minimize the impact of accumulation of errors and roughness in the deposition process.

Considering an MLL as a volume grating in which the thickness of the optic is much greater than the layer spacings, diffraction can be described (locally) by dynamical diffraction [18, 20, 25]. The condition for Bragg diffraction is illustrated in Fig. 1(a), where rays are reflected from layers if they obey Bragg's law, $\lambda = 2\,d\,\sin\theta$ for a layer period d. In addition to the Bragg-diffracted beam, there is a forward-refracted beam as depicted in Fig. 1(b). This beam can be considered as a zero order diffraction although unlike in the kinematic diffraction approximation this beam is refracted by the MLL structure. Higher diffracting orders do exist, but the MLL must be tilted into a different orientation to observe them [21]. They may be observed simultaneously with the other two beams when the MLL period is not significantly smaller than the thickness along the optical axis, such as in the low-resolution portion of the lens (close to the optical axis) [18].

Optics EXPRESS

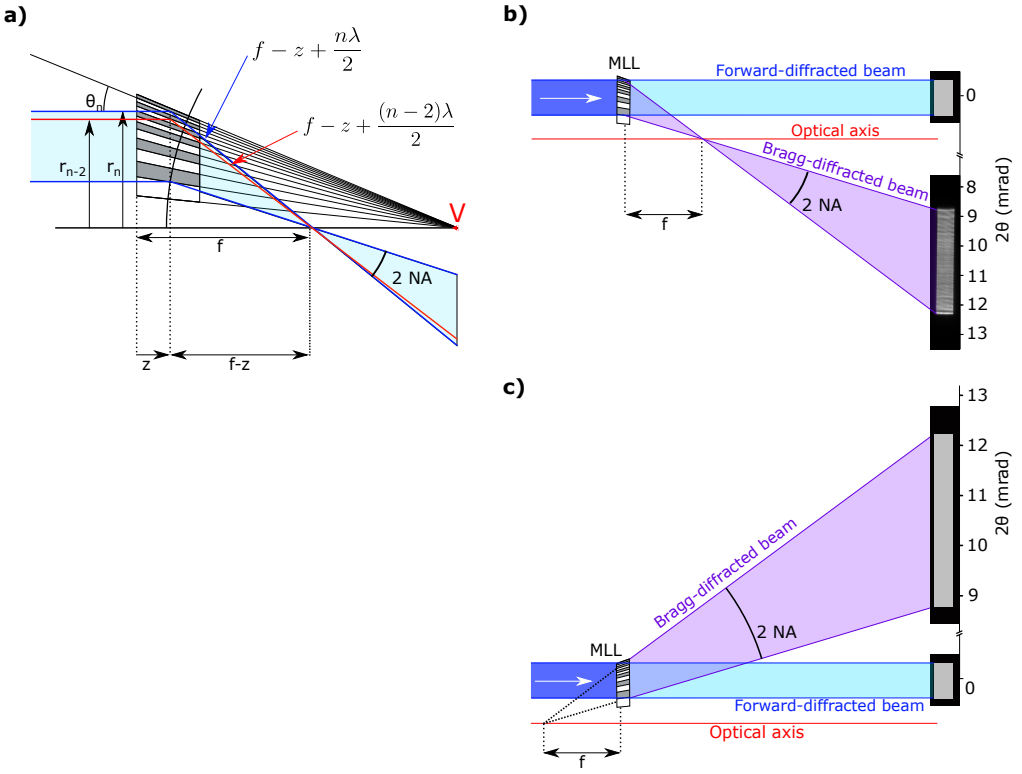

Fig. 1. (a) Schematic of a wedged MLL. The blue and red lines depict rays that are reflected in the lens at a distance z ($z \ll f$) from the entrance of the MLL. The upper incident blue ray is reflected by the n^{th} layer, while the red ray is reflected two layers below it ($n-2$), but the heights r_n and r_{n-2} ensure the ray paths differ by a wavelength and add in phase at the focus. The layers are oriented azimuthally on a circle centered at the vertex V. (b) Schematic showing an incident collimated beam (darker blue) diffracted into two beams by the wedged MLL, when the lens is oriented in the Bragg-diffracting condition. The direct beam transmits through the MLL (light blue beam) without change of direction (it is attenuated and refracted). The Bragg-diffracted beam converges on the focus and diverges thereafter (purple beam). The measured far field intensity of the Bragg-diffracted beam of a wedged MLL is depicted. (c) Schematic of the Bragg-diffracting condition for an incident collimated beam parallel to the optic axis when the MLL is rotated so that the wedge vertex is upstream of the lens.

For a wedged MLL, only the forward-refracted and Bragg-diffracted focused beams are excited across the entire pupil, when the lens is in the diffracting condition. The forward beam occurs for all tilts of the structure but its transmission is reduced when light is instead directed into the Bragg-diffracting beam. The fraction of light directed into either the forward or Bragg-diffracting beam oscillates with the thickness of the structure, referred to as the Pendellösung effect [25]. The efficiency of the Bragg-diffracting beam is optimized at a thickness equal to half a Pendellösung period (see Eq. (21) in [20]). As discussed below, efficiencies greater than 80 % may be achieved.

The Bragg-diffracting beam is divergent, rather than convergent, when the lens is flipped around so that the beam is incident from the opposite face as shown in Fig. 1(c). That is, the vertex of the layers (point V in Fig. 1) is upstream of the lens. In this case the rays reflect from the opposite sides of the layers and the diverging beam appears to originate from a point a distance f in front of the lens. The diffraction efficiency of this diverging beam is equal to that of the

Optics EXPRESS

converging beam.

Table 1. List of MLL design parameters for the lenses used in this paper*.

Name	Photon energy (keV)	f (mm)	D (μm)	Number of layers	NA ($\times 10^{-3}$)	Optical thickness (μm)	Multilayer materials	d_{min} (nm)	FOV (μm)
1h	17.3	9.5	37.2	11350	2	7.0	WC/SiC	7.31	9.5
1v	17.3	13.7	43.5	12778	1.6	6.5	WC/SiC	7.13	15.1
2h	34.5	37	31.6	6612	0.4	8.5	W/SiC	8.47	22.2
2v	34.5	40	55.7	16502	0.7	9.0	WC/SiC	6.01	27.2

*f is the focal length, D is the physical aperture size, d_{min} the minimum layer period, and FOV the field of view which is calculated as FOV $\approx f\Delta\theta$, where $\Delta\theta$ is the Darwin width.

A one-dimensional MLL fabricated by deposition on a flat substrate acts as a cylindrical lens, focussing X rays only in one direction. Imaging or focusing in two dimensions requires two crossed MLLs, oriented to focus in orthogonal directions (e.g. horizontally and vertically). This is analogous to two cylindrical lenses or the two focusing mirrors in a Kirkpatrick-Baez system. The two MLLs must be optimized for the same photon energy but manufactured with focal lengths whose difference is equal to the separation of the lenses, so that they focus in both directions to a common point. As with crossed cylindrical lenses or mirrors, the focal length is different in the two directions, and thus so too is the magnification of an image formed with this configuration. This is known as an anamorphic lens system. Depending on the physical aperture of each MLL (which can be varied independently of focal length) the lens system may have a square or rectangular pupil function. For a square or rectangular pupil the point spread function is the product of two orthogonal sinc-functions. Using the Rayleigh criterion, the spatial resolution $\Delta_{h,v}$ is equal to $\Delta_{h,v} = 0.5\lambda/\mathrm{NA}_{h,v}$. The constant factor (0.5) corresponds to the first zero of the sinc-function of the point spread function [26].

Each MLL is actually fabricated as an off-axis portion of a cylindrical lens, with the thickest (last deposited) layer being some distance from the optical axis. As shown in Fig. 1(b), this allows the forward beam to be separated from the Bragg-diffracted focused beam of each lens. When operating together, each in their diffracting condition, the two crossed MLLs form four beams altogether: a forward-refracted beam; a horizontal line focus from the Bragg-diffracting beam of the vertically-focusing lens with the forward-refracted beam of the other; a vertical line focus from the opposite combination of orders; and the two-dimensionally focused beam. All four beams become spatially separated at a plane between the lens and the focus, where an L-shaped beam block may be placed to prevent off-axis regions of a sample to be exposed (similar to an order-sorting aperture used in scanning microscopes with thin zone plates [7]). In the far field (of the focus) the two line foci diverge into linear diffraction orders and the two-dimensional focus diverges into the inverted (square or rectangular) pupil of the lens pair.

The ability to manufacture the thin layers required for high numerical apertures depends on both the deposition process control and on the materials used. In the study presented here we used WC/SiC throughout, except for one MLL with a smaller NA, where we used W/SiC. The WC/SiC system is a novel material combination with many beneficial properties [27]. In a previous study a focused spot size of 8.4 nm × 6.8 nm [13] at 16.3 keV was achieved with MLLs consisting of WC/SiC. Both WC and SiC remain amorphous over the whole range of the layer periods, avoiding wavefront errors that arise due to a transition from an amorphous to a crystalline structure in the W layers [21]. The multilayers used here were prepared in DESY's X-ray multilayer deposition

Optics EXPRESS

laboratory as described previously [21, 28]. Each MLL was cut from a multilayer prepared in a separate deposition run; hence, four different deposition runs were required for two energies and two sets of 1D lenses. Design pameters of the MLLs are listed in Table 1. For both sets the MLL with the shorter focal length was mounted to focus the beam horizontally, while the one with a longer focal length focused the beam vertically. We name the lenses designed for 17.3 keV "1h" (horizontally focusing) and "1v" (vertically focusing). The MLLs of the set used at 34.5 keV are named "2h" and "2v".

The optimal lens thickness depends on the photon energy and on the contrast of the optical constants of the multilayer materials. The volume fraction of the high atomic-number material in each bilayer of the multilayer, denoted here as Γ, and the layer period d have only a weak influence on the optimal lens thickness [20]. The optimal thickness can be calculated from dynamical diffraction calculations [20] or multislice beam propagation simulations [29, 30]. These calculations were performed for $\Gamma = 0.5$ and optical constants were determined based on materials densities of the deposited materials obtained by fitting small angle X-ray diffraction scans of periodic multilayers [27]. These densities were $\rho_{\mathrm{W}} = 19.3\,\mathrm{g\,cm^{-3}}$, $\rho_{\mathrm{WC}} = 13.8\,\mathrm{g\,cm^{-3}}$ and $\rho_{\mathrm{SiC}} = 2.64\,\mathrm{g\,cm^{-3}}$, where the subscripts indicate the material. They are lower than the known bulk densities of these materials of $\rho_{\mathrm{WC,bulk}} = 15.6\,\mathrm{g\,cm^{-3}}$ and $\rho_{\mathrm{SiC,bulk}} = 3.21\,\mathrm{g\,cm^{-3}}$ [31]. At 17.3 keV photon energy an optimum diffraction efficiency of 59 % was obtained for a 7.5 µm thick WC/SiC MLL, and at 34.5 keV an optimum diffraction efficiency of 85 % was obtained for a 12.2 µm thick W/SiC MLL. Due to positioning errors in the FIB preparation process the actual optical thicknesses of the MLLs for horizontal and vertical focusing at 17.3 keV were 7.0 µm and 6.5 µm, respectively, giving a computed efficiency of 31 %. The optical thicknesses of the MLLs for horizontal and vertical focusing at 34.5 keV were 8.5 µm and 9.0 µm, respectively. These thinner lenses are computed to have efficiencies of about 78 %.

3. Experimental

3.1. Experimental setup

Experiments for lens characterization and for the applications presented in this paper were performed at the beamline ID06 at the European Synchrotron Research Facility (ESRF, Grenoble, France). The beam was monochromatized to 17.3 keV or 34.5 keV by a Si (111) double crystal monochromator in Bragg-Bragg geometry and subsequently pre-focused with a CRL transfocator consisting of a stack of eight 2D-focussing Be lenses with 100 µm radius of curvature, placed 38.7 m downstream from the source. The end station was located approximately 58 m downstream from the source and offered a highly stable setup due to an underlying granite block with a mass of 20 tons. A CRL with 25 2D-focussing Be lenses with an apex radius of curvature of 50 µm and a distance between lenslets of 2 mm was placed as a condenser before the MLLs to increase the flux. The resulting focal length at 17.3 keV was 0.78 m.

The vertically and horizontally focusing MLLs were located on the same mount, which could be oriented to match two configurations. In the first configuration, the MLLs focused the incident beam to a spot (an image of the source), requiring the $2f$ wedge to converge in the downstream direction. This is the usual arrangement for scanning microscopy, although employed here primarily for wavefront characterization of the lenses and for projection microscopy. We refer to this as the "nanoprobe" configuration. In the "full-field imaging" configuration the MLLs were rotated by 180° such that the wedge apex was in the upstream direction for efficient acceptance of rays scattered from an object located slightly upstream of the focal plane of the lens. The mount could be further translated in three directions and rotated about two axes (pitch and yaw). The alignment of the lenses was carried out in the nanoprobe configuration. To align the MLLs relative to each other, the MLL with the longer focal length (vertically focusing) was placed on a hexapod (on the common mount), with six degrees of freedom. The hexapod had a repeatability of 15 nm for up to 1 mm travel range. A first detector was located 0.13 m downstream from the

Optics EXPRESS

MLLs to record transmission images of the MLLs. This detector comprised a scintillator screen coupled by a visible light microscope to a Frelon 2k CCD camera. The effective pixel size was 1.24 µm. A second, similar detector using a pco.2000 CCD camera, was placed 0.41 m or 0.63 m downstream from the MLLs and was used for recording the X-ray microscopy images (Fig. 2). This was also a scintillator-based detector with a 10× objective, which resulted in an effective pixel size of 0.74 µm.

3.2. Imaging geometries

We explored the use of the MLLs for projection imaging and for direct imaging where the lens forms a magnified image of the object on the detector. Projection imaging was carried out in two different geometries: one with a real source and one with a virtual source. The three geometries are illustrated in Figs. 2(a)–2(c).

3.2.1. Projection holography with a real source

A projection image or a Gabor hologram of an object may be obtained by placing it into the diverging spherical wave that propagates beyond the focused spot created by the MLL in the nanoprobe configuration. The divergence magnifies the projected hologram so that features much smaller than a detector pixel can be discerned. The divergence also allows the projection hologram to be recorded in the near field. The resolution to which an image can be reconstructed depends in this case on the extent of the secondary source formed by the MLLs [32].

In this work, we used this mode of imaging for wavefront characterization as described below. Specifically, the sample was located a distance L_1 downstream of the focus and the intensity distribution was recorded on the detector located a distance L_2 from the sample, with a magnification of 78 given by the geometric factor $M = (L_1 + L_2)/L_1$. The measured Fresnel diffraction pattern of the object's transmission $\Psi(\vec{r})$ formed with the diverging spherical wave is equivalent to that formed by plane-wave illumination of a magnified object $\Psi(\vec{r}/M)$ but recorded a distance ML_2 from the object [33]. The Fresnel number of the diffraction of an object of width w is thus equal to $(Mw)^2/(\lambda ML_2)$. In our measurements, $L_2 = 400$ mm, $M = 78$, giving a Fresnel number of 960 for an object of width of 19 µm and wavelength of 0.72 Å (17.3 keV). For lens alignment and aberration characterization the lenses were first positioned to obtain a common focus, eliminating horizontal-vertical astigmatism. This was achieved by first roughly adjusting the distance between the lenses to give equal magnification of the projection hologram in the vertical and horizontal directions, and then further adjustment was carried out by sensing the wavefront through the method of speckle tracking [34]. Furthermore, the orthogonal astigmatism aberration (45°-astigmatism) was reduced by aligning the roll of the horizontal lens located on the hexapod [15] until the images of the line diffraction orders were orthogonal to each other, using the orthogonality of the pixels of the detector as the reference. However, the line diffraction orders recorded on the detector have a width equal to the physical aperture size of the respective MLL, which can be up to 59 pixels for the investigated MLLs. Consequently, a residual deviation from 90° between the transverse focusing directions is still present after aligning (see Section 4.2).

3.2.2. Projection holography with a virtual source

Projection images can also be obtained when the lenses are rotated by 180° to be oriented in the full-field configuration depicted in Fig. 2(b), where the apexes of the lens wedges lay upstream of the lenses. An incident collimated beam parallel to the optical axis, Bragg-diffracts from each lens into a diverging beam, operating as a lens of negative power as described in Sec. 2. Since the beam is diverging, a magnified projection image can be recorded on a downstream detector, just as described in Sec. 3.2.1. This is convenient for the characterisation and alignment of lenses arranged in the full-field configuration using the same speckle-tracking method mentioned above.

Optics EXPRESS

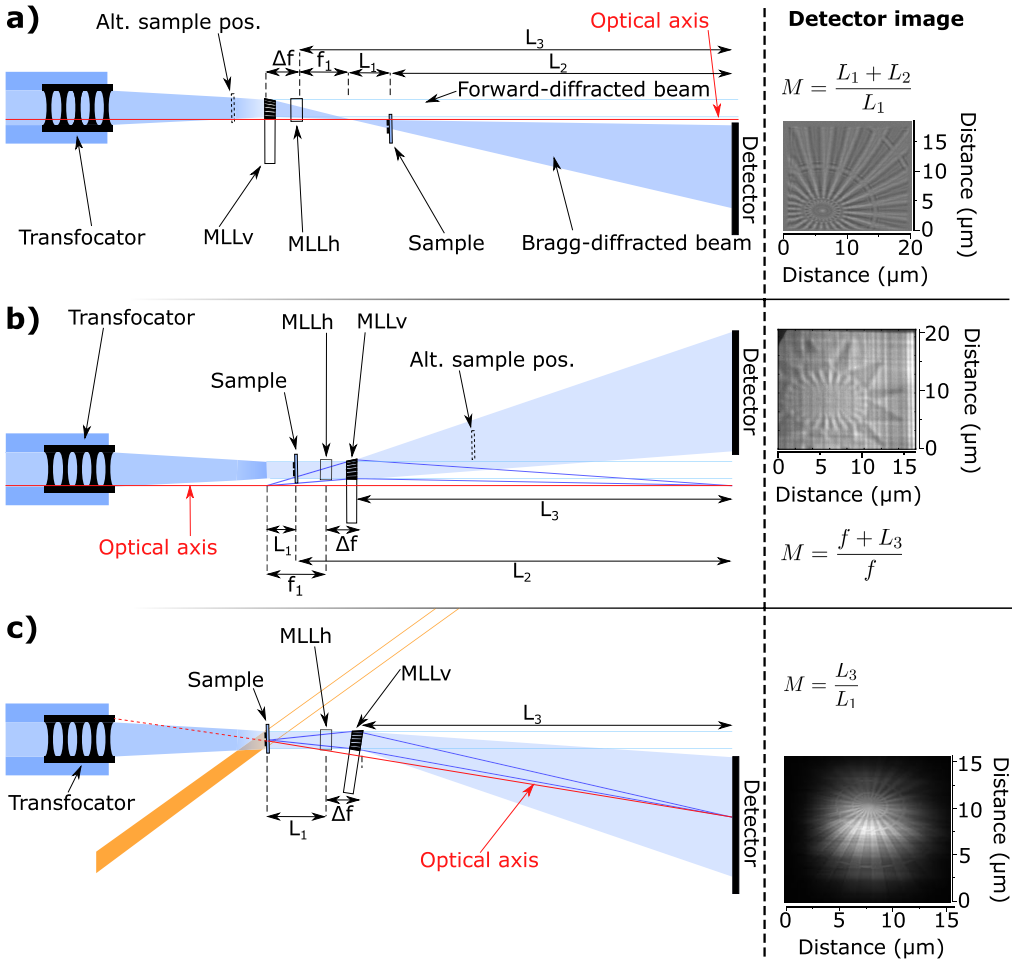

Fig. 2. Three kinds of imaging modes were used in two configurations of the MLLs. In the "nanoprobe" configuration the vertices of the MLL wedges lie downstream of the lens (a) and in the "full-field" configuration they lie upstream (b, c). (a) A sample placed in the diverging beam downstream of beam focus in the nanoprobe configuration forms a projection hologram. Alternatively, the sample can be placed upstream of the lenses (Alt. sample pos.). (b) Another projection holography mode is obtained in the "full-field" configuration where a collimated incident beam parallel to the optical axis is Bragg-diffracted into the diverging beam depicted in Fig. 1(c). The sample may again be placed upstream of the MLL (as shown) or downstream (Alt. sample pos.). Rays (shown in blue) originating from an object in a small field near the optics axis satisfy the Bragg condition of the focused beam to form a magnified direct image. (c) In the direct imaging mode with bright-field illumination, the lens is tilted so that the incident rays pass both through the object field and the lens aperture. Rays (shown in blue) originating from the object satisfy the Bragg condition of the focused beam to form a magnified direct image. In dark-field direct imaging, the incoming beam (orange) is directed away from the lens aperture and the scattered rays (blue) are Bragg-diffracted by the MLL. The right column shows cropped detector images obtained in the respective configurations. For all depicted configurations, the sample was a Siemens star and distances on the detector image axes refer to object space.

Optics EXPRESS

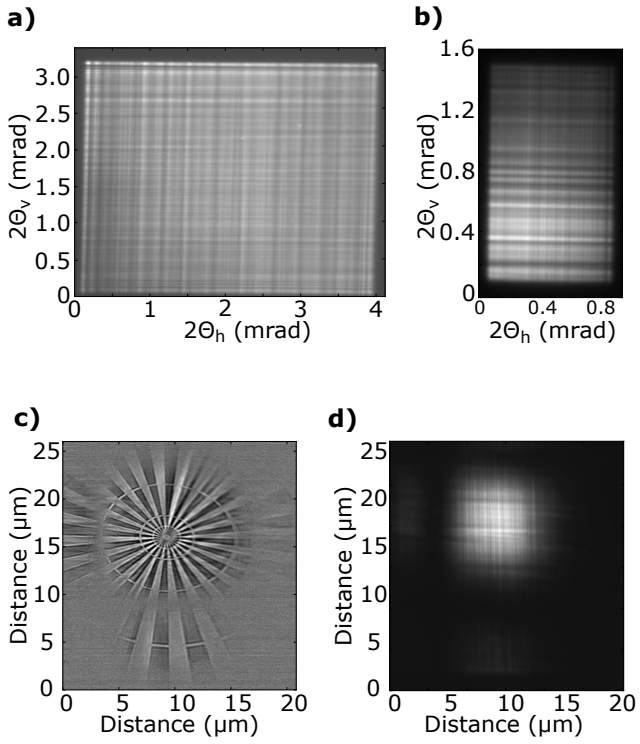

Fig. 3. The intensity of the lens pupil in the projection imaging configuration of Fig. 2(a) at (a) 17.3 keV and at (b) 34.5 keV. The horizontal and vertical axes are the horizontal diffraction angle $2\theta_h$ and the vertical diffraction angle $2\theta_v$, respectively. A flat-field corrected bright-field real image of a test object at 17.3 keV is depicted in (c). The intensity of the field at 17.3 keV without the sample present is shown in (d), with an extent that is smaller than the FOV of the image of an object. The axes in both (c) and (d) are distances in object space. For all intensity plots the grey scale is linearly scaled between 0 counts (black) and the maximum intensity (white).

Similar to projection holography with a real source, an object can be placed downstream or upstream of the lens to form a magnified projection hologram. With the object placed downstream of the lens, the magnification is as described above and given by $M = (L_1 + L_2)/L_1$ where now L_1 is the distance of the object to the virtual focus. Again, the diffraction distance for the equivalent "standard" collimated-beam diffraction geometry, is ML_2. The lenses can be roughly brought into a confocal alignment by ensuring that the horizontal and vertical magnifications of the projection image are equal.

When the object is located upstream of the lens and illuminated by a collimated beam, as depicted in Fig. 2(b), then the diffraction is in fact initially "standard" and reaches each lens while still in the near field (apparent since the field width is set by the lens aperture). The action of each lens is to expand this diffraction by a factor $M = (L_3 + f)/f$ (where L_3 is the lens to detector distance) and to give a further propagation that, together with the first, would be equivalent to diffraction of the magnified object propagated over a distance $M^2L_1 + ML_3$. Even though $L_3 + f$ are equal for the two lenses when they are aligned to be confocal, the magnification of the projection image is different in each direction due to the different distances that the diffraction from the object propagates to the respective lens. Figure 2(b) shows a projection hologram of a Siemens star.

Optics EXPRESS

Note that when operating as a negative lens for an incident parallel beam, the wedged MLL can simultaneously form a real inverted image of an object close to the optical axis with the positive (converging) Bragg-diffracted beam. This is shown for the blue rays in Fig. 2(b). Since the MLLs are designed with a $2f$ wedge (for focusing a collimated beam), such direct imaging is optimized for forming a real image at infinity (with the object located a focal distance from the lens). However, the angular acceptance of the diffracting layers of the MLLs allows for efficient diffraction from rays originating from positions slightly away from the focus as well (see also the discussion below in Sec. 3.2.3 about the field of view). Thus, high magnifications can be tolerated. The direct image is centered on the optical axis and thus does not overlap with the projection hologram formed using the Bragg-diffracted diverging beam. The image will actually be a dark-field image since the incident illumination passing through the object, parallel to the optical axis, will not pass through the off-axis aperture of the MLLs. That is, the zero spatial frequency of the object lies outside the entrance pupil of the lens.

3.2.3. Direct imaging

The ability for the lens to form a direct image when the wedge vertices are located upstream is indeed why we refer to this as the "full-field" configuration. As we have seen, the wedge of the lenses breaks the symmetry found in non-wedged MLLs, which requires considerations beyond prior investigations of full-field imaging using MLLs [35]. In general, when used to form a real magnified image of an object, the lenses will not be placed to fulfill the diffraction condition of the diverging beam for the incident illumination, but rather adjusted to achieve the desired imaging conditions for light scattering from the object. This direct imaging configuration is illustrated in Fig. 2(c). Here, just as for a thin lens, the image is inverted with respect to the optical axis, even though the MLLs are formed as off-axis portions of full lenses. The image is anamorphic due to the different focal lengths of the two MLLs. Taking each lens to be an ideal thin lens (neglecting its thickness), in our studies, the horizontal magnification was $M_h = 635\,\mathrm{mm}/9.5\,\mathrm{mm} \approx 67$ and the vertical magnification $M_v = 630\,\mathrm{mm}/13.7\,\mathrm{mm} \approx 46$.

The contrast of the image depends on the illumination. Figure 2(c) shows that bright-field or dark-field direct imaging can be realized, depending on whether the incident beam illuminating the object (within the field of view close to the optical axis) is directed into the entrance pupil of the lens or not. In the case of bright-field microscopy the contrast depends mostly on the transmission of the object since the optical transfer function of the lens overlaps the zero spatial frequency of the object. By moving the sample slightly out of focus, phase contrast is obtained (defocus contrast). In dark-field imaging, only rays scattered by the sample into the entrance pupil of the MLLs form the image, which excludes the zero spatial frequency. The details of the image formation depend on the coherence of the illumination [36]. For hard X rays, we are particularly interested in forming images from X rays Bragg-scattered from crystallites in the sample which happen to be oriented in the appropriate reflecting condition [37]. This requires setting the illumination angle (in practice, tilting the optical axis of the lens) to match the chosen Bragg angle.

A key feature of an MLL objective used in the direct imaging mode is that the diffraction properties of the lens cause vignetting of the image field. The layers are oriented to reflect rays originating from a point in the object (with an object to lens distance L_1 slightly larger than f) on the optical axis. Rays originating from points in the sample plane further away from the optical axis will be diffracted by particular layers in the lens with less efficiency, as those rays move out of the rocking-curve acceptance of the layers. This acceptance varies with the position on the lens. For the small diffraction angles of MLLs this Darwin width varies inversely with the Bragg angle [25, 38] and thus it is linearly proportional to the layer period, as well as being proportional to the difference in optical constants of the layers [20]. Thus, as the object point moves away from the optical axis, the effective NA of the lens is reduced as more layers (starting

Optics EXPRESS

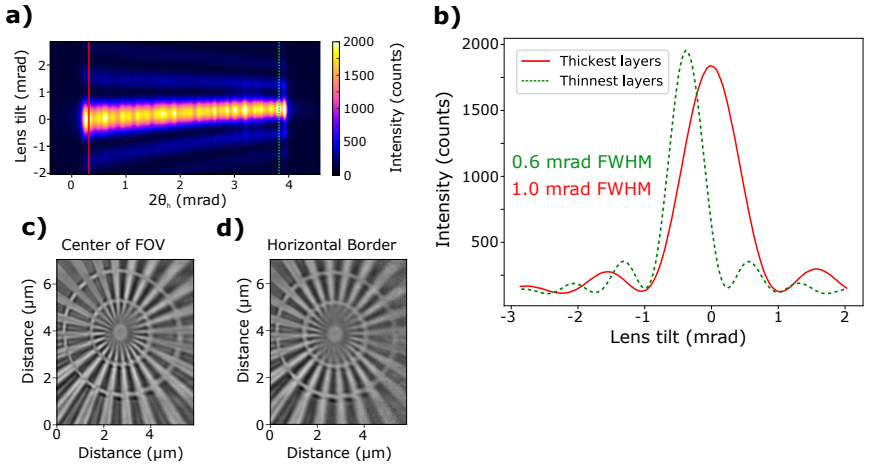

Fig. 4. (a) Diffraction efficiency as a function of the pupil position ($2\theta_h$) and lens tilt for MLL lens 1h measured at 17.3 keV. (b) Plots of diffraction efficiency for the parts of the MLL with the thickest layers (red solid line) and for the thinnest layers (green dashed line). (c) Cropped full field image of the center of the Siemens star test sample, for which the features were located at the center of the FOV. (d) The same sample features after moving the sample to the horizontal edge of the FOV, while still being centered in the vertical direction.

from the thinnest) exclude rays. The extent of the field is ultimately limited by the acceptance of the thickest layers. The full aperture of the lens, and hence the full resolution, is only achieved within the acceptance of the thinnest layers, with the field of view depending on the Darwin width $\Delta\theta$ as FOV $= L_1\Delta\theta \approx f\Delta\theta$. The vignetting is analogous to that of an ideal thin lens of finite NA with an entrance pupil located between the object and the lens, such that the full NA of the lens is only achieved for a point on axis. The FOVs of the investigated MLLs, obtained from the measured Darwin width, can be found in Table 1. An experimental quantification of this effect and its impact on the imaging resolution is given in Section 4.1 (Fig. 4).

4. Optical performance

4.1. Basic performance of the MLLs

Image formation in a microscope can be described by Fourier optics [39]. A coherent full-field image, formed for example by illumination of a transmitting sample by a collimated beam, is given by the square modulus of the convolution of the object's transmission function and the point spread function of the lens [39]. The point spread function in this case is the Fourier transform of the complex-valued lens pupil function, which ideally should be of uniform amplitude and phase within the angular acceptance of the lens. Note that due to the vignetting described above, the pupil function varies with the position of the point in the field, and the formalism of Fourier optics holds over a limited region called the isoplanatic patch.

In the nanoprobe configuration, a map of the square modulus of the lens pupil function for the on-axis field point can be obtained simply from the far-field diffraction pattern recorded on the detector without any object in place, as formed using collimated illumination parallel to the optical axis. (The pupil for other points in the field can be obtained by carrying out the same procedure with different lens tilts.) As shown in Fig. 3, the pupil intensities for 17.3 keV and 34.5 keV show a checkerboard pattern. Apart from this pattern the pupil intensity of the set (1h,1v) are uniform at 17.3 keV, indicating constant efficiency as seen in Fig. 3(a). The pupil intensity of the set (2h,2v) at 34.5 keV shows an intensity gradient with highest intensity in the

Optics EXPRESS

bottom left corner (in Fig. 3(b)). This intensity gradient is attributed to a slight mismatch of the optimal photon energies for the individual MLLs of the set (2h,2v). The rectangular pupil shape (instead of a square) in Fig. 3(b) is due to the difference in the numerical apertures of the used MLLs (0.4×10^{-3} (2h) versus 0.7×10^{-3} (2v); see Table 1).

A bright-field direct image of a test object at 17.3 keV is depicted in Fig. 3(c) for magnifications of 67 in the horizontal direction and 46 for the vertical. The Siemens star pattern is made from 600 nm thick gold, and with 50 nm smallest features. Anamorphism of the image is clearly seen. The magnifications would suggest an anamorphism of $67/46 = 1.49$, which matches the observed anamorphism of 1.4 ± 0.1. The field of view is finite, and the image vignetting caused by the finite angular acceptance of the MLLs is seen to follow the shape of a distorted sinc function with visible side lobes along the horizontal and vertical axes. The illumination without the sample (flat field) is shown in Fig. 3(d). This illumination alone is smaller than the field of view of the lenses: it is the rays scattered by the object and which appear to originate from a region near the optical axis at the object plane that fulfil the Bragg condition in the lens and which contribute to the image, whereas the incident rays that pass through the image plane near the edge of the field of view do not sastisfy the Bragg condition. This is another consequence of the vignetting of the lens, and again the analogy is fitting to a thin lens with a limiting aperture placed between the lens and object (especially considering that we use an off-axis portion of the lens).

Figure 4(a) shows the measured diffraction efficiency of the Bragg-diffracted beam (obtained in the nanoprobe configuration), mapped as a function of the lens tilt, for the horizontally focusing MLL designed for 17.3 keV (1h). The measured widths are 1.0 mrad FWHM for the thickest layers and 0.6 mrad for the thinnest layers. With a focal length of 9.5 mm, this corresponds to a FOV at the object plane of 9.5 µm and 5.7 µm, respectively for these layers. That is, we would expect full resolution to be achieved over a FOV of 5.7 µm. Figs. 4(c) and 4(d) show cropped full field images of the finest features of the Siemens star test sample. For Fig. 4(c), the sample was moved so that the features were in the center of the FOV and therefore could be imaged with optimal resolution. In Fig. 4(d), the sample was moved horizontally to place the features at the horizontal border of the FOV, while the vertical side was still centered. The vertical resolution (as seen by the sharpness of the horizontal lines) was unaffected by this sample shift, while the horizontal resolution (the sharpness of the vertical lines) was worse due to the lower effective NA. This confirms the vignetting behavior described in Sec. 3.2.3. The overall FOV of the investigated MLLs, obtained from the measured Darwin width, can be found in Table 1.

4.2. Wavefront characterization and resolution

We carried out wavefront measurements to characterize the aberrations of the MLLs by two different methods: ptychography [40–42] and speckle tracking [34, 43]. Both methods were carried out in the "nanoprobe" configuration. For the (1h,1v) MLLs at 17.3 keV, near-field ptychography was performed using a gold Siemens star pattern placed 1010 µm downstream of the focus. For speckle tracking the defocus was increased to 5.8 mm and near-field projection holograms were recorded for different transverse positions of the object. An iterative speckle tracking algorithm was used to recover the wavefront aberration and the corrected projection hologram of the object. Even for perfectly manufactured MLLs, astigmatism may be present in the lens system due to misalignment of the lenses. The 0-90°-astigmatism occurs if the two MLLs are not confocal, and 45°-astigmatism occurs if the lenses are not orthogonal to each other [14, 15]. When analyzing the aberrations, astigmatism and defocus are therefore subtracted. This can be done by defining a set of Legendre polynomials that are orthogonal on a rectangular pupil, similar to Zernike polynomials on a unit disk. As the calculations are performed on a finite grid, the numerical polynomials are not perfectly orthogonal. To overcome this, a numerical Gram-Schmidt orthogonalization is carried out [44]. If the two MLLs are perfectly orthogonal then the wavefront will be separable such that the phase across the pupil can

Optics EXPRESS

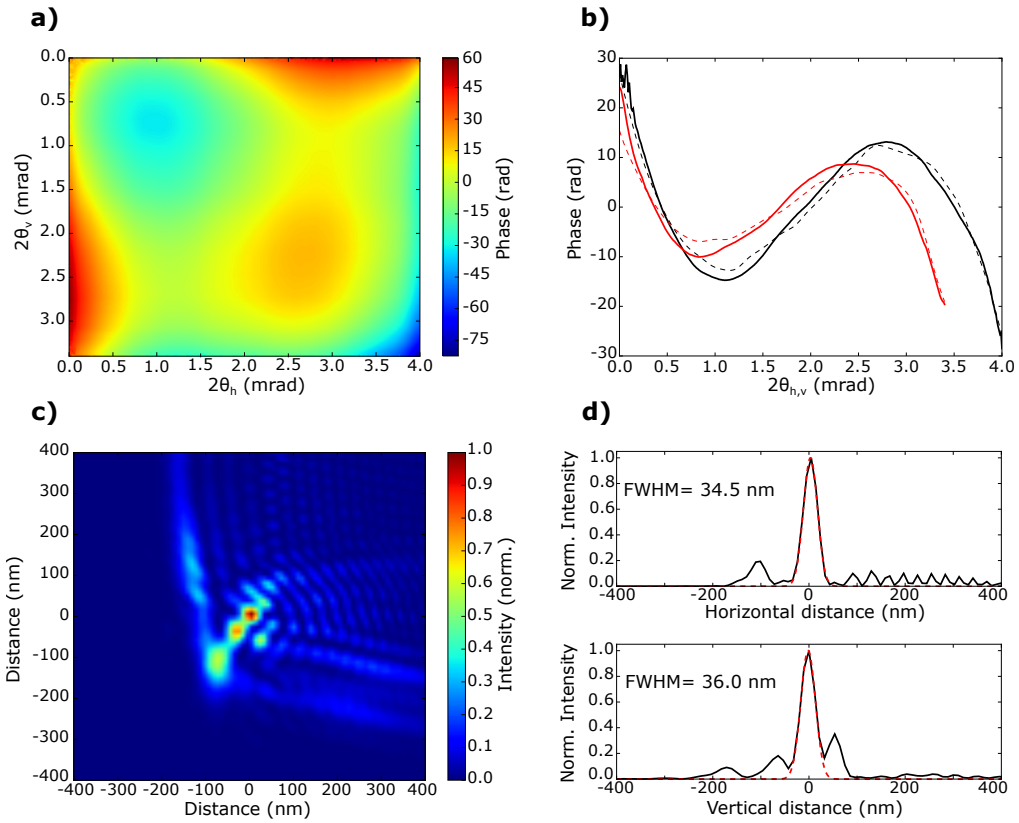

Fig. 5. Wavefront characterization at 17.3 keV. (a) 2D wavefront retrieved from ptychography after removing primary aberrations of focus and astigmatism. (b) The separated horizontal and vertical wavefronts after removing 45° astigmatism. The black curves show the horizontal phase profile and the red curves show the vertical profile. The solid lines are the results from ptychography and the dashed lines were obtained from speckle tracking. (c) The intensity in the focal plane according to ptychographic reconstructions. (d) The horizontal and vertical profiles of the focal-plane intensity.

be written as $\phi(x, y) = \phi_h(x) + \phi_v(y)$. Nevertheless, the measurement indicated a small residual 45°-astigmatism due to a slight non-orthogonality of the lenses [15], of about 0.2°. Only after removing this 45°-astigmatism, could the wavefronts be separated.

The reconstructed wavefront aberrations of the (1h,1v) lens pair at 17.3 keV are displayed in Fig. 5 as obtained via ptychography and speckle tracking, with good agreement between these two methods. The resulting separated phase profiles $\phi_h(x)$ and $\phi_v(y)$ are plotted in Fig. 5(b). The shape of the aberration is similar to coma. Similar aberrations were reported previously for an unrelated set of MLLs and can be attributed to a systematic error in the deposition rate [13]. For the horizontally focusing MLL (1h), the measured phase error is approximately 60 rad peak to valley, accumulated over 6000 layers and corresponding to about a 5 % change in the required deposition rate. For periods of about 10 nm, the error per period is approximately 0.5 nm. The point spread function of the MLL set is shown in Fig. 5(c) along with the horizontal and vertical lineouts in Fig. 5(d). By fitting the central spot with a Gaussian function, FWHM widths of (34 ± 2) nm and (36 ± 3) nm were obtained for the horizontal and vertical directions, respectively, listed in Table 2. These values agree well with a focus size of (35 ± 5) nm obtained by analyzing the edge sharpness in the full field image. Unaberrated lenses of the NA used here would have a

Optics EXPRESS

Table 2. Focal length, focus size (FWHM) and efficiency of the investigated MLLs.

Name	Energy (keV)	f (mm)	Theoretical spatial resolution (nm)	Experimental focal length (nm)	Theoretical efficiency (%)	Experimental efficiency (%)
1h	17.3	9.5	18	34.5 ± 1.5	59	51
1v	17.3	13.7	22	36 ± 3.0	58	54
2h	34.5	37	40	114 ± 7	77	n.a.
2v	34.5	40	23	56 ± 11	79	n.a.

Rayleigh resolution of 18 nm horizontal and 22 nm in the vertical. It may be possible to correct for much of the aberration by appropriate modification of the deposition parameters to achieve close to these calculated resolutions.

At 34.5 keV (lenses 2h,2v), the reduced coherence and reduced absorption and scattering contrast of the Au test sample (compared with 17.3 keV) prevented any meaningful result to be obtained by ptychography. It was still possible to track features in the near-field projection hologram, however, to obtain wavefront measurements by speckle tracking. The 1D wavefront obtained for the horizontal lens was worse than that of the vertical, giving a Gaussian fit to the recovered point spread function of (114 ± 7) nm in the horizontal direction and (56 ± 11) nm in the vertical direction. The optimal Rayleigh resolution of diffraction limited MLLs for the given NA is 40 nm and 23 nm (see Table 2).

4.3. Diffraction efficiency

The diffraction efficiencies of the MLLs were estimated by measuring the extinction of the lenses [45] in the "nanoprobe" configuration', using the "Frelon 2k" camera. (Extinction can also be measured in the "full-field" configuration.) When the MLL is tilted into the Bragg-diffracting condition, the transmission of the forward beam is significantly reduced, because most of the rays diffract away from the detector. This effect is illustrated in Fig. 6. The number of photons diffracted into the focused beam compared with the number in the incident beam is then estimated as the change in the transmission of the lens in the forward direction: $E = (I_{\mathrm{nb}} - I_{\mathrm{b}})/(I_0 - I_{\mathrm{det}})$, where I_{nb} is the measured counts per second when the lens is out of the Bragg condition, I_{b} is the same with the lens in the Bragg condition, I_0 is the incident counts (measured to the side of the shadow of the lens), and I_{det} is the detector signal with the beam off. This definition assumes that all the beam diffracted out of the forward direction contributes to the focused beam, which is to say that it does not account for any other diffraction orders that may be simultaneously excited. Measurements of the far-field diffraction did not detect any such orders other than some diffuse scattering accounting for less than 1 % of the photons. The resulting efficiencies are listed in Table 2 for the lens set (1h,1v). The efficiencies of the other set were not measured. The diffraction efficiencies at 17.3 keV were 51 % and 54 %, giving a combined efficiency for the two-dimensional focus of 27.3 %, slightly lower than the theoretical value of 34 %. We attribute this loss in efficiency to a non-optimum wedging of the layers as indicated in the rocking-curve measurement shown in Fig. 4(a).

5. Demonstration of direct imaging

In the past, several successful demonstrations of the use of MLLs for projection microscopy were made at X-ray energies of 9 to 12 keV [45, 46], and one previous study was performed on direct imaging using MLLs [35]. In this section, we demonstrate the use of the MLLs for magnified

Optics EXPRESS

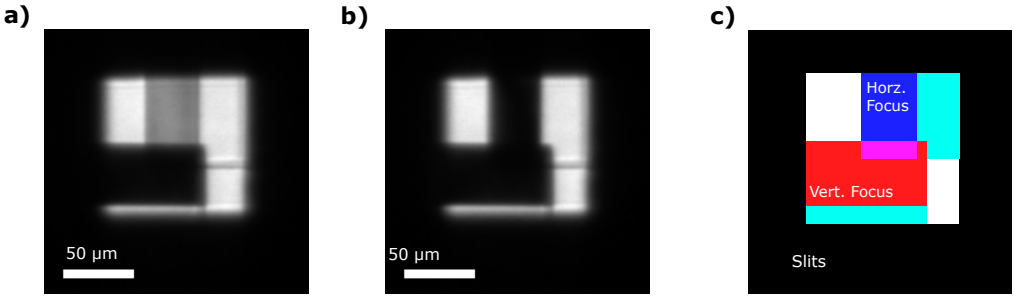

Fig. 6. (a) and (b) Detected maps of the X-ray transmission through the two MLLs at 17.3 keV. The slits were opened to reveal the incident beam and the lenses were slightly displaced from their overlapping condition. The vertically-focusing MLL is in the Bragg-diffracting condition. A schematic is shown in (c) with the vertically-focusing MLL indicated by the red rectangle, the horizontally-focusing MLL indicated by the blue rectangle, and their overlap in purple. Both lenses were mounted on silicon substrates, depicted as cyan squares. In (a) the horizontally-focusing MLL was tilted away from the Bragg condition and in (b) set to the Bragg condition.

direct bright-field imaging as illustrated in Fig. 2(c). The proof-of-concept study relates directly to the vision of 3D multiscale materials science pursued at the hard X-ray microscope ID06 at ESRF. Here the resolution-limiting element currently is the X-ray objective. For studies above 20 keV, CRLs [47–49] have been the optics of choice. Aberrations in CRLs have limited the achievable resolution to approximately 100 nm. In comparison, MLLs with reduced manufacturing errors, a higher NA and a higher efficiency open the door to local imaging with a much-improved spatial resolution.

Figures 7(a)–7(c) present flat-field corrected bright-field images of a Siemens star object recorded at 17.3 keV using different amounts of defocus obtained by adjusting the position of the MLL set along the optical axis. The horizontal magnification was 67 and the vertical magnification was 46. The images are displayed without correcting for this anamorphism, but this can be done simply by scaling the picture. (Anamorphism is not an aberration such as field distortion, the effect is equivalent to measuring with a detector with rectangular pixels.) Other parameters of the lens set (1h,1v) are given in Table 1. The width of the field of view was measured to be approximately 7 µm FWHM, comparable with the predicted value of 9.5 µm. The images clearly document the feasibility of the use of MLLs for direct beam imaging. Astigmatism can be observed in the images, for example by comparing the contrast of the inner-most spokes in Figs. 7(a) and (b). This aberration is due to an incorrect spacing between the two lenses. However, the lenses also exhibit a high degree of coma, as shown in the wavefront map and line-outs of Figs. 5(a) and (b). The dominant phase error in each lens varies with the third power of the coordinate x (i.e. coma) and the lens pair gives a sum $\phi_h(x) + \phi_v(x)$ that is dominated by a coma oriented at 45° as is also apparent in Fig. 5(c). This coma gives better resolution in the images in Fig. 7 of the Siemens star pattern along the lines that are oriented at 45°.

It is illustrative to compare the optical specifications of this setup to the equivalent setup with a Be CRL as objective. For the same focal length and magnification, and with the available specifications of a radius of curvature of 50 µm and a thickness of 2 mm, such an objective would require the use of 157 lenslets, be 31 cm long, have an NA of 0.42×10^{-3} and a FOV of 87 µm RMS [37]. As with MLLs, there exists a trade off between NA and FOV.

Translating the lens pair along the optical axis gives rise to fringes in both the vertical and horizontal directions around the edges of the spokes of the Siemens star object, as seen in Figs. 7(a)–7(c). This is consistent with defocus phase contrast, including the reversal of the

Optics EXPRESS

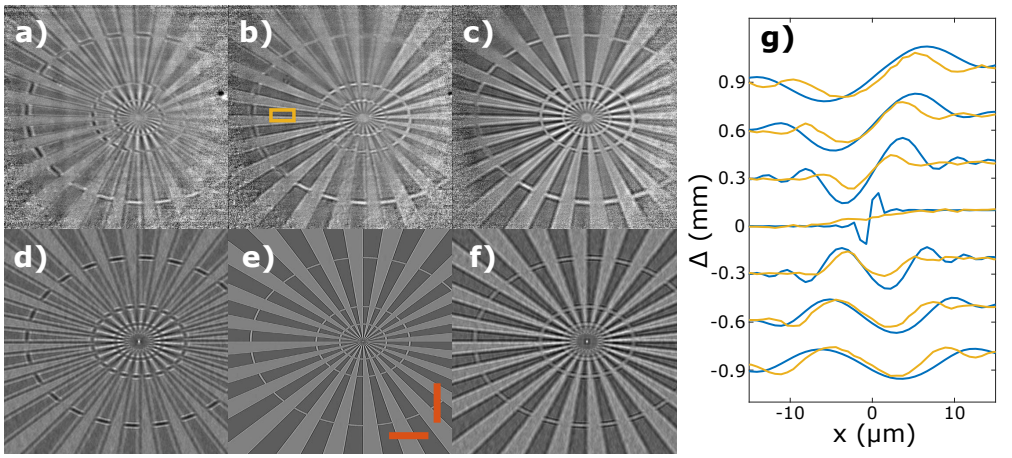

Fig. 7. Bright-field direct imaging of the Siemens star with the MLL objective being translated along the optical axis. (a-c) Experimental images for defocus distances of 0.6 mm, 0 mm, and −0.6 mm relative to the best focus for the region depicted by the light-orange box. (d-f) Corresponding partial coherent wavefront simulations with the same three distances. The orange scale bars in (e) are 2 μm in the object plane. (g) Vertical line profiles obtained from the position indicated by the yellow box in (b). The seven curves correspond to relative sample-objective distances of −0.9 mm, −0.6 mm, −0.3 mm, 0 mm, 0.3 mm, 0.6 mm, and 0.9 mm, respectively, with the shortest distance at the bottom. Corresponding simulations with a vertical coherence length of 130 nm are shown in blue.

contrast of the fringes on opposite sides of focus. This can be observed, for example, in the region indicated by the light-orange box in Fig. 7(b). To quantify the contrast, we performed a set of partially coherent wavefront simulations for each position of the MLLs, replicating the experiment in the simulations, see Figs. 7(d)–7(f). The wavefront simulations were performed using a Fractional Fourier Transform approach [50]. We initially computed the exit field on transmission through the Siemens star based on a fully coherent incoming plane wave, calculating the attenuation and phase shift corresponding to the 600 nm thick Au features of the object. The wavefront propagation simulations took only the astigmatism into account. The wavefront propagation model captures the main features of the experiment, in particular the reversal of fringe contrast, but the experimental contrast was less pronounced than the simulations. This may be an indication that the incoming beam was only partially coherent, and therefore we introduced a horizontal and vertical coherence length into the simulations. By optimizing the correspondence between experiment and model, the estimated values of these coherence lengths are 65 nm and 130 nm respectively. As an example of the results, in Fig. 7(g) we compare the intensity profiles across a horizontal edge. Although the simulations do not account for all aberrations, the agreement of the experimental and simulated profiles, and particularly the diminished contrast in focus, indicates that defocus causes the change in contrast in these images.

These results point to a new way of performing high resolution phase contrast studies with hard X rays, compared with the projection holography discussed in Secs. 3.2 and 4.2. These approaches give complementary trade-offs between FOV and resolution. Phase retrieval for a set of images taken through focus may be obtained using solutions based on the transport of intensity equation [51]. Notably, for the set-ups demonstrated here it is not required to place any optical elements or a detector close to the sample to probe the nearfield, and when employed in the direct-imaging configuration, phase contrast can be easily combined with diffraction-contrast imaging.

Optics EXPRESS

6. Conclusions

Multilayer Laue lenses are particularly promising high-resolution optical elements for hard X-ray photons extending even beyond photon energies of 100 keV. Here we demonstrated their use in X-ray microscopy experiments at 17.3 keV and 34.5 keV. A detailed lens characterization was performed in a projection imaging geometry. The pair of wedged MLLs designed for 17.3 keV focused the beam to (35 ± 2) nm horizontally and (36 ± 3) nm vertically, with an efficiency of 51 % × 54 %. The wavefront of these lenses was obtained by two different methods: ptychography and by speckle tracking. The results show good qualitative and quantitative agreement. Speckle tracking does not have strict coherence requirements, making it suitable for sensing the wavefront of the focused beam produced by a set of MLLs at 34.5 keV. This characterization indicated a focus size of (114 ± 7) nm horizontal and (60 ± 10) nm vertical. Retrieved wavefronts of all investigated MLLs showed a high reproducibility of the residual wavefront curvature, caused by systematic errors in the materials deposition, which can presumably be corrected in future lenses.

After successful characterization of the MLLs, we realized bright-field and dark-field direct-imaging microscopy set-ups, using the MLLs as an objective to form a magnified image. It was shown that the field of view of the microscope was limited to approximately 9.5 µm × 15.1 µm for the investigated set of MLLs designed for 17.3 keV and to 22.2 µm × 27.2 µm for the 34.5 keV objective. The FOV is proportional to the focal length but is limited by the finite angular acceptance of the layers, or the Darwin width of the diffracting structure, which is inversely proportional to the d-spacing of the structure. Hence, there is a compromise between large FOV and high resolution in the design of such a microscope. Furthermore, we demonstrated defocus phase contrast imaging with bright-field illumination. Contrast was limited, however, by the beam coherence. Fractional Fourier Transform simulations were used to replicate the experimental conditions, which enabled us to estimate the horizontal and vertical coherence lengths of the incoming beam at 65 nm and 130 nm. Compared with CRLs, which are the state of the art optics at high energies for applications such as dark-field microscopy, MLLs potentially offer higher spatial resolutions, higher angular coverage (or NA) and higher-speed imaging due to high focusing efficiency.

Funding

Deutsche Forschungsgemeinschaft (DFG) (Gottfried Wilhelm Leibniz Program, Cluster of Excellence "Advanced Imaging of Matter"—EXC 2056—project ID 390715994); DanMAX (4059-00009B); European Research Council advanced grant (ERC) (291321 d-TXM); European Research Council synergy grant (609920 AXSIS); travel grant by Danish instrument center Danscatt.

Acknowledgments

We would like to thank Sabrina Bolmer and Pavel Alexeev (DESY) for their help and technical support, Andrzej Andrejczuk (Univ. of Bialystok, Poland) for helpful and constructive discussions and ESRF for provision of beamtime. C. D. thanks D. M. Paganin for stimulating discussions on the field of view of thick lenses.

References

1. G. E. Ice, J. D. Budai, and J. W. L. Pang, "The race to X-ray microbeam and nanobeam science," Science **334**, 1234–1239 (2011).
2. J. C. Andrews and B. M. Weckhuysen, "Hard X-ray spectroscopic nano-imaging of hierarchical functional materials at work," ChemPhysChem **14**, 3655–3666 (2013).
3. E. Maire and P. J. Withers, "Quantitative X-ray tomography," Int. Mat. Rev. **59**, 1–43 (2014).
4. H. Simons, A. King, W. Ludwig, C. Detlefs, W. Pantleon, S. Schmidt, F. Stöhr, I. Snigireva, A. Snigirev, and H. F. Poulsen, "Dark-field X-ray microscopy for multiscale structural characterization," Nat. Commun. **6**, 6098 (2015).

Optics EXPRESS

5. T. A. Lafford, J. Villanova, N. Plassat, S. Dubois, and D. Camel, "Synchrotron X-ray imaging applied to solar photovoltaic silicon," J. Phys. Conf. Ser. **425**, 192019 (2013).
6. O. Betz, U. Wegst, D. Weide, M. Heethoff, L. Helfen, W., K., Lee, P., and Cloetens, "Imaging applications of synchrotron X-ray phase-contrast microtomography in biological morphology and biomaterials science. I. General aspects of the technique and its advantages in the analysis of millimetre-sized arthropod structure," J. Microsc. **227**, 51–71 (2007).
7. D. T. Attwood and A. Sakdinawat, *X-rays and Extreme Ultraviolet Radiation: Principles and Applications* (Cambridge University, 2016), 2nd ed.
8. T. Wilson and C. Sheppard, *Theory and Practice of Scanning Optical Microscopy* (Academic, London, 1984).
9. A. G. Michette, *Optical Systems for Soft X rays* (Plenum, 1986), p. 59.
10. J. C. da Silva, A. Pacureanu, Y. Yang, S. Bohic, C. Morawe, R. Barrett, and P. Cloetens, "Efficient concentration of high-energy X-rays for diffraction-limited imaging resolution," Optica **4**, 492–495 (2017).
11. Y. Suzuki, "Resolution Limit of Refractive Lens and Fresnel Lens in X-Ray Region," Jpn. J. Appl. Phys. **43**, 7311–7314 (2004).
12. H. C. Kang, J. Maser, G. B. Stephenson, C. Liu, R. Conley, A. T. Macrander, and S. Vogt, "Nanometer linear focusing of hard X rays by a multilayer Laue lens," Phys. Rev. Lett. **96**, 127401 (2006).
13. S. Bajt, M. Prasciolu, H. Fleckenstein, M. Domaracký, H. N. Chapman, A. J. Morgan, O. Yefanov, M. Messerschmidt, Y. Du, K. T. Murray, V. Mariani, M. Kuhn, S. Aplin, K. Pande, P. Villanueva-Perez, K. Stachnik, J. P. Chen, A. Andrejczuk, A. Meents, A. Burkhardt, D. Pennicard, X. Huang, H. Yan, E. Nazaretski, Y. S. Chu, and C. E. Hamm, "X-ray focusing with efficient high-NA multilayer Laue lenses," Light: Sci. Appl. **7**, 17162 (2018).
14. H. Yan and Y. S. Chu, "Optimization of multilayer Laue lenses for a scanning X-ray microscope," J. Synchrotron Radiat. **20**, 89–97 (2013).
15. H. Yan, X. Huang, N. Bouet, J. Zhou, E. Nazaretski, and Y. S. Chu, "Achieving diffraction-limited nanometer-scale X-ray point focus with two crossed multilayer Laue lenses: alignment challenges," Opt. Express **25**, 25234–25242 (2017).
16. R. M. Bionta, K. M. Skulina, and J. Weinberg, "Hard X-ray sputtered-sliced phase zone plates," Appl. Phys. Lett. **64**, 945–947 (1994).
17. T. Liese, V. Radisch, and H.-U. Krebs, "Fabrication of multilayer Laue lenses by combination of pulsed laser deposition and focused ion beam," Rev. Sci. Instrum. **81**, 073710 (2010).
18. H. Yan, J. Maser, A. Macrander, Q. Shen, S. Vogt, G. B. Stephenson, and H. C. Kang, "Takagi-Taupin description of X-ray dynamical diffraction from diffractive optics with large numerical aperture," Phys. Rev. B **76**, 115438 (2007).
19. H. N. Chapman and A. V. Rode, "Geometric optics of arrays of reflective surfaces," Appl. Opt. **33**, 2419–2436 (1994).
20. S. Bajt, H. N. Chapman, A. Aquila, and E. Gullikson, "High-efficiency X-ray gratings with asymmetric-cut multilayers," J. Opt. Soc. Am. A **29**, 216–230 (2012).
21. A. J. Morgan, M. Prasciolu, A. Andrejczuk, J. Krzywinski, A. Meents, D. Pennicard, H. Graafsma, A. Barty, R. J. Bean, M. Barthelmess, D. Oberthuer, O. Yefanov, A. Aquila, H. N. Chapman, and S. Bajt, "High numerical aperture multilayer Laue lenses," Sci. Rep. **5**, 9892 (2015).
22. R. Conley, C. Liu, J. Qian, C. M. Kewish, A. T. Macrander, H. Yan, H. C. Kang, J. Maser, and G. B. Stephenson, "Wedged multilayer Laue lens," Rev. Sci. Instrum. **79**, 053104 (2008).
23. M. Prasciolu, A. F. G. Leontowich, J. Krzywinski, A. Andrejczuk, H. N. Chapman, and S.Bajt, "Fabrication of wedged multilayer Laue lenses," Opt. Mat. Express **5**, 228318 (2015).
24. X. Huang, R. Conley, N. Bouet, J. Zhou, A. Macrander, J. Maser, H. Yan, E. Nazaretski, K. Lauer, R. Harder, I. K. Robinson, S. Kalbfleisch, and Y. S. Chu, "Achieving hard X-ray nanofocusing using a wedged multilayer Laue lens," Opt. Express **23**, 12496–12507 (2015).
25. A. Authier, *Dynamical Theory of X-Ray Diffraction* (Oxford University, 2001).
26. M. Born and E. Wolf, *Principles of Optics* (Cambridge University, 2002), 7th ed.
27. M. Prasciolu and S. Bajt, "On the Properties of WC/SiC Multilayers," Appl. Sci. **8**, 571 (2018).
28. S. Bajt, M. Prasciolu, A. J. Morgan, H. N. Chapman, J. Krzywinski, and A. Andrejczuk, "One dimensional focusing with high numerical aperture multilayer Laue lens," AIP Conf. Proc. **1696**, 020049 (2016).
29. A. Andrejczuk, J. Krzywinski, and S. Bajt, "Influence of imperfections in a wedged multilayer Laue lens for the focusing of X-rays investigated by beam propagation method," Nucl. Instr. Meth. Phys. Res. B **364**, 60–64 (2015).
30. K. Li, M. Wojcik, and C.Jacobsen, "Multislicing does it all— calculating the performance of nanofocusing X-ray optics," Opt. Express **25**, 1831–1846 (2017).
31. W. M. Haynes, *CRC Handbook of Chemistry and Physics* (CRC, 2011), pp. 4.96 and 4.88, 92nd ed.
32. C. T. Koch, "Towards full-resolution inline electron holography," Micron **63**, 69–75 (2014).
33. A. Papoulis, *Systems and Transforms with Applications in Optics* (McGraw-Hill, 1968), 1st ed.
34. S. Bérujon, E. Ziegler, R. Cerbino, and L. Peverini, "Two-dimensional X-ray beam phase sensing," Phys. Rev. Lett. **108**, 158102 (2012).
35. S. Niese, P. Krüger, A. Kubec, S. Braun, J. Patommel, C. G. Schroer, A. Leson, and E. Zschech, "Full-field X-ray microscopy with crossed partial multilayer Laue lenses," Opt. Express **22**, 20008–20013 (2014).
36. S. Vogt, H. N. Chapman, C. Jacobsen, and R. Medenwaldt, "Dark field X-ray microscopy: the effects of condenser/detector aperture," Ultramicroscopy **87**, 25–44 (2001).
37. H. F. Poulsen, A. C. Jakobsen, H. Simons, S. R. Ahl, P. K. Cook, and C. Detlefs, "X-ray diffraction microscopy based

Optics EXPRESS

on refractive optics," J. Appl. Cryst. **50**, 1441–1456 (2017).
38. J. Als-Nielsen and D. McMorrow, *Elements of Modern X-ray Physics* (Wiley, 2011), 2nd ed.
39. J. W. Goodman, *Introduction to Fourier Optics* (McGraw-Hill, 1996).
40. H. N. Chapman, "Phase-retrieval X-ray microscopy by Wigner deconvolution," Ultramicroscopy **66**, 153–172 (1996).
41. J. Vila-Comamala, A. Diaz, M. Guizar-Sicairos, A. Mantion, C. M. Kewish, A. Menzel, O. Bunk, and C. David, "Characterization of high-resolution diffractive X-ray optics by ptychographic coherent diffractive imaging," Opt. Express **19**, 21333–21344 (2011).
42. A. Kubec, S. Braun, S. Niese, P. Krüger, J. Patommel, M. Hecker, A. Leson, and C. G. Schroer, "Ptychography with multilayer Laue lenses," J. Synchrotron Radiat. **21**, 1122–1127 (2014).
43. M.-C. Zdora, "State of the art of X-ray speckle-based phase-contrast and dark-field imaging," J. Imaging **4**, 60 (2018).
44. F. J. Koch, C. Detlefs, T. J. Schröter, D. Kunka, A. Last, and J. Mohr, "Quantitative characterization of X-ray lenses from two fabrication techniques with grating interferometry," Opt. Express **24**, 9168–9177 (2010).
45. H. Yan, V. Rose, D. Shu, E. Lima, H. C. Kang, R. Conley, C. Liu, N. Jahedi, A. T. Macrander, G. B. Stephenson, M. Holt, Y. S. Chu, M. Lu, and J. Maser, "Two dimensional hard X-ray nanofocusing with crossed multilayer Laue lenses," Opt. Express **19**, 15069–15076 (2011).
46. X. Huang, W. Xu, E. Nazaretski, N. Bouet, J. Zhou, Y. S. Chu, and H.Yan, "Hard X-ray scanning imaging achieved with bonded multilayer Laue lenses," Opt. Express **25**, 8698–8704 (2017).
47. A. Snigirev, V. Kohn, I. Snigireva, and B. Lengeler, "A compound refractive lens for focusing high-energy X-rays," J. Opt. Soc. Am. **384**, 49–51 (1996).
48. C. G. Schroer, O. Kurapova, J. Patommel, P. Boye, J. Feldkamp, B. Lengeler, M. Burghammer, C. Riekel, L. Vincze, A. van der Hart, and M. Küchler, "Hard X-ray nanoprobe based on refractive X-ray lenses," Appl. Phys. Lett. **87**, 124103 (2005).
49. G. B. M. Vaughan, J. P. Wright, A. Bytchkov, M. Rossat, H. Gleyzolle, I. Snigireva, and A. Snigirev, "X-ray transfocators: focusing devices based on compound refractive lenses," J. Synchrotron Radiat. **18**, 125–133 (2011).
50. A. F. Pedersen, H. Simons, C. Detlefs, and H. F. Poulsen, "The fractional Fourier transform as a simulation tool for lens-based X-ray microscopy," J. Synchrotron Radiat. **25**, 717–728 (2018).
51. L. J. Allen and M. P. Oxley, "Phase retrieval from series of images obtained by defocus variation," Opt. Comm. **199**, 65–75 (2001).